Homaeigohar, Shahin; Tsai, Ting Yu; Zarie, Eman S.; Elbahri, Mady; Young, Tai Horng; Boccaccini, Aldo R.

Bovine Serum Albumin (BSA)/polyacrylonitrile (PAN) biohybrid nanofibers coated with a biomineralized calcium deficient hydroxyapatite (HA) shell for wound dressing

Published in:
Materials Science and Engineering C

DOI:
10.1016/j.msec.2020.111248

Published: 01/11/2020

Document Version
Publisher's PDF, also known as Version of record

Materials Science & Engineering C 116 (2020) 111248

Contents lists available at ScienceDirect

Materials Science & Engineering C

journal homepage: www.elsevier.com/locate/msec

Bovine Serum Albumin (BSA)/polyacrylonitrile (PAN) biohybrid nanofibers coated with a biomineralized calcium deficient hydroxyapatite (HA) shell for wound dressing

Shahin Homaeigohar[a,b,*], Ting-Yu Tsai[c], Eman S. Zarie[b,d], Mady Elbahri[b], Tai-Horng Young[c], Aldo R. Boccaccini[a]

[a] Institute of Biomaterials, Department of Materials Science and Engineering, University of Erlangen-Nuremberg, 91058, Erlangen, Germany
[b] Nanochemistry and Nanoengineering, Department of Chemistry and Materials Science, School of Chemical Engineering, Aalto University, Kemistintie 1, 00076 Aalto, Finland
[c] Institute of Biomedical Engineering, College of Medicine and College of Engineering, National Taiwan University, Taipei 100, Taiwan
[d] Department of Therapeutical Chemistry, Pharmaceutical and Drug Industries Research Division National Research Centre, Dokki 12311, Giza, Egypt

ARTICLE INFO

Keywords:
Polyacrylonitrile (PAN)
Nanofiber
Biofunctionalization
Biomineralization
Wound dressing

ABSTRACT

Here, for the first time, a nanofibrous (NF) wound dressing comprising biomineralized polyacrylonitrile (PAN) nanofibers is developed. In contrast to the majority of the currently available nanofibrous wound dressings that are based on natural polymers, PAN is a synthetic, industrial polymer, which has been rarely considered for this purpose. PAN NFs are first hydrolyzed to allow for tethering of biofunctional agents (here Bovine Serum Albumin (BSA)). Later, the biofunctionlized PAN NFs are biomineralized by immersion in simulated body fluid (SBF). As a result, core-shell, calcium deficient hydroxyapatite (HA)/BSA/PAN nanofibers form, that are mechanically stronger (elastic modulus; 8.5 vs. 6 MPa) compared to the untreated PAN NFs. The biomineralized PAN NFs showed promising bioactivity as reflected in the cell biology tests with fibroblast and keratinocyte cells. Hs68 fibroblasts and HaCat keratinocytes were found to be more viable in the presence of the biomineralized NFs than when they were co-cultured with the neat PAN NFs. Such mechanical and biological characteristics of the biomineralized PAN NFs are favorable for wound dressing applications.

1. Introduction

Wound dressings are an important sector of the medical and pharmaceutical wound care market worldwide. The global market of these products is expected to reach $20.4 billion by 2021 from $17.0 billion in 2016, due to ascending of the aging population and related increase of the incidence of chronic diseases such as diabetes [1].

Wound dressings must protect the wound, remove exudate, inhibit exogenous microorganism invasion and improve wound appearance [2]. An ideal dressing creates an optimal healing environment wherein healing progresses at an acceptable rate with respect to recovery of the wound appearance. Among the different categories of wound dressing materials, electrospun nanofibers (NFs) can provide wound dressing scaffolds suitable to promote cell attachment and proliferation. At the same time, they offer anesthetic and antibiotic activity for pain relief and healing, respectively [3].

In comparison to the golden benchmark for wound dressings i.e. films, foams, fibrous and meshes, NF dressings are more porous thus allowing more efficient oxygen and water permeability, nutrient exchange and removal of metabolic waste. In addition, their notably higher surface area and biomimicry of the extracellular matrix favor cell attachment, proliferation and differentiation during tissue regeneration [4]. Meanwhile, nanoscale fibers, conferring the dressing with small interstices and a high surface area can enhance hemostasis. Not only does the small pore size of NF dressings protect the wound against bacterial infection, but also can NF dressings provide excellent conformability, thus offering a better coverage and protection of wounds from infection [5].

While the majority of research on NFs for wound dressings has focused on the natural polymeric building blocks including collagen, chitosan, etc., synthetic industrial NFs could offer distinct advantages such as optimum physicochemical properties, low cost, easy processability, adaptability to industrial technologies, and scalability [6]. These engineering aspects are of paramount importance considering the

* Corresponding author at: School of Science and Engineering, University of Dundee, Dundee DD1 4HN, United Kingdom.
E-mail address: shahin.homaeigohar@fau.de (S. Homaeigohar).

https://doi.org/10.1016/j.msec.2020.111248
Received 2 May 2020; Received in revised form 29 June 2020; Accepted 29 June 2020
Available online 02 July 2020

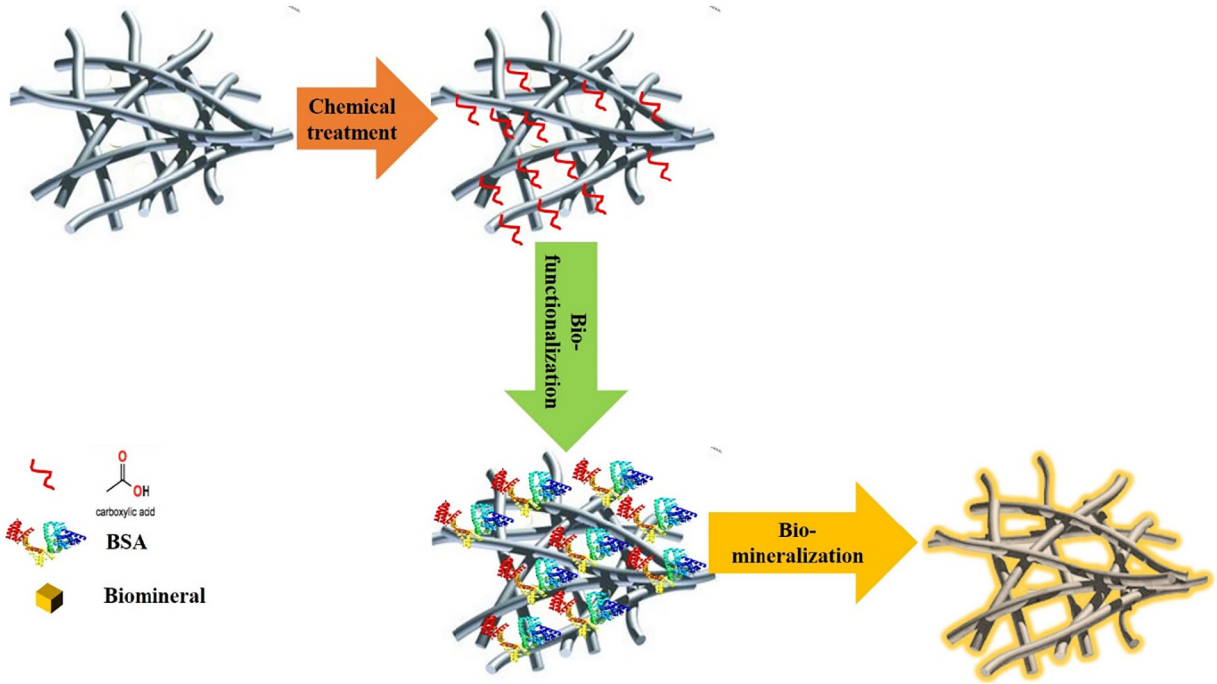

Fig. 1. The sequences of chemical treatment, biofunctionalization and eventually biomineralization of PAN NFs.

translation and the need for commercialization of such products.

In the literature, various NF wound dressings have been reported based on synthetic polymers. In such systems, the polymer is either blended with natural polymers or bio-derived compounds or is reinforced by incorporation of nanoparticles. Examples for the biohybrid class include the NFs made of polyvinyl alcohol (PVA) blended with chitosan [7] and with alginate and honey [8]. Ag nanoparticle incorporated polycaprolactone (PCL) NFs [9] are also an example of the nanocomposite NFs proposed for wound dressing application. Despite optimum structural properties, one main concern regarding the synthetic polymers that can be suggested for NF wound dressings is the lack of cellular interactivity and biocompatibility. Noteworthy, to address the dynamic nature of wound healing, the wound care market is transitioning from classic protective barriers to advanced, active wound dressings, which interact with the wound by stimulating and managing cell migration and the sequence of healing events. This bottleneck of synthetic polymers can be addressed via biomineralization of their surface to induce a bioactivity effect and biomimicry.

In nature, biomineralization is the process whereby living creatures from prokaryotes to human induce the precipitation of minerals and create multiplex inorganic structures. These structures are biohybrids, composed of biologic (or organic) and inorganic compounds, in a given ratio, depending on their formation medium [10]. Mimicking naturally biomineralized systems, synthetic bionanohybrids are an emerging class of nanostructured organic-inorganic materials. They are made of biopolymers (e.g. proteins) and inorganic solids (e.g. minerals) with at least one dimension on the nanometer scale [11]. The biocompatibility of the biopolymer guarantees the applicability of such hybrid nanostructures in the biomedical field. Also, the inorganic component adds extra functionalities e.g. hydrophilicity, bioactivity, and optical, magnetic, etc. properties.

The multifunctionality of bionanohybrids is indeed a promising research topic that exploits the advantage of the synergistic assembling of biopolymers with an inorganic nanoscaled phase. Here, we developed a biomineralization process for polyacrylonitrile (PAN) NFs and investigated the new hybrid structures with respect to structural properties and biocompatibility when in contact with cells typically found in the wound milieu. PAN is a synthetic thermoplastic polymer with optimum solvent and chemical resistance, and high mechanical properties [12]. PAN is commonly used to fabricate a plethora of products such as fibers for textiles, ultra-filtration membranes, etc. As fiber, PAN is typically employed for production of high- quality carbon fibers [13].

2. Materials and methods

2.1. Materials

PAN, with the molar mass of 200,000 $g{\cdot}mol^{-1}$, was purchased from Dolan GmbH (Germany). The solvent *N*,*N*-dimethylformamide (DMF) and NaOH were obtained from Merck (Germany). Bovine Serum Albumin (BSA) (dried powder) with the molecular weight of 66,430 (A2153, dried powder, CAS No.9048-46-8) and Phosphate Buffered Saline (PBS) were purchased from Sigma-Aldrich Co. All the materials were used as received.

2.2. Sample preparation and modification

The PAN NF mats were produced via the electrospinning method. Briefly, a prepared PAN solution (8 wt% (w/w) in DMF) was fed with a constant rate of 0.8 $ml{\cdot}h^{-1}$ into a needle by using a syringe pump (Harvard Apparatus, USA). By applying a given voltage of 15 kV (Heinzinger Electronic GmbH, Germany), PAN was electrospun on an aluminum foil, located at a distance of 25 cm from the needle. The PAN NFs were collected after 8 h continuous electrospinning at ambient temperature and ambient relative humidity of 70–75% and dried at a temperature of 100 °C by a vacuum oven overnight to exclude any residual solvent.

In the next step, the PAN NFs were hydrolyzed in a NaOH aqueous solution (1 N) for 2 h at 60 °C. Such a chemical post treatment was aimed to functionalize the NFs by replacing their nitrile groups with hydroxyl and carboxyl ones [14]. To raise biocompatibility of the hydrolyzed NFs, they were biofunctionalized. The induced –COOH groups on PAN will readily enable formation of ionic and covalent bonds with amine groups of protein ligands [15]. In order to biofunctionalize the NFs, the hydrolyzed NFs were immersed in a BSA/PBS solution

(5 mg·ml^{-1}) and heated for 5 h at 50 °C. The as-treated NFs were left as immersed in the BSA solution overnight, then washed with PBS three times and air dried.

For the sake of biomineralization, the biofunctionalized NFs were immersed in simulated body fluid (SBF) (10 ml) prepared according to the standard procedure described by Kokubo et al. [16], and placed in a shaking incubator (Heidolph Unimax10-10, Germany) at 37 °C for 2 days. Subsequently, the NFs were thoroughly washed by deionized water and air dried at room temperature. Fig. 1 schematically illustrates the procedure of chemical treatment, biofunctionalization and eventually biomineralization of the PAN NFs (hereafter called as c-PAN, b-PAN, and bm-PAN, respectively).

2.3. Characterizations of structural properties

The morphology of PAN NFs as neat and biomineralized was characterized by scanning electron microscopy (SEM) (LEO 1550VP Gemini from Carl ZEIS, Germany). The exudate uptake capacity of the NF mats as neat, functionalized and biomineralized was calculated based on their weight gain at specific time intervals, when immersed in an exudate mimicking solution. For this purpose, a solution simulating wound exudate was prepared by adding 0.368 g calcium chloride (Sigma Aldrich, USA) and 8.298 g sodium chloride (Sigma Aldrich, USA) to water (1 l), following a standard protocol [17]. The solution was vigorously stirred for homogenizing. Thereafter, the NF samples were immersed in the solution at 37 °C and weighed after 1, 3, and 7 h to determine their exudate uptake ability through the following Eq. (1):

$$W_g = \frac{W_t - W_0}{W_0} \times 100 \quad (1)$$

where W_g, W_0, and W_t are weight gain (uptake capacity), primary and momentary weight of the NF samples before and after immersion in the solution.

The tensile properties of the NF samples (1 cm × 2 cm × 0.1 cm) were tested by a uniaxial tensile tester (Bose ElectroForce 5500, TA instruments, Delaware, USA). At least 5 samples of each group were tested. To calculate the porosity, 3 cuboid NF samples of each category of the PAN NFs with given dimensions (thus volume) were weighed using an electronic balance (precision of 0.1 mg). The apparent density (ρ_0) of the samples was determined from the obtained mass and volume. The porosity (ε) was then quantified via the following Eq. (2) [18]:

$$\varepsilon = \frac{(\rho_0 - \rho)}{\rho_0} \times 100\% \quad (2)$$

where ρ is the bulk density of PAN (1.184 g/cm^3 [19]).

Porosity of the bm-PAN NF mats was also determined by the ImageJ software to compare with that obtained through the Eq. (2).

Surface chemistry of the PAN NFs was determined by ATR-FTIR (ALPHA (ATR-Ge, ATR-Di) from BRUKER Optik GmbH, Ettlingen, Germany). Structural analysis of the biomineralized PAN NFs was carried out at room temperature using an X-ray diffractometer (Miniflex 600, Rigaku, Japan) with Cu-Kα radiation (= 0.15418 nm).

2.4. Characterizations of biological properties

Fibroblast viability was evaluated through the WST-1 assay. Hs68 cells (ATCC, Manassas, VA) were cultured in DMEM (ThermoFisher Scientific, MA) supplemented with 10% fetal bovine serum and 1% streptomycin/penicillin. The cell suspension was placed in the cell culture incubator (95% relative humidity, 5% CO_2 and 37 °C). After trypsinization, Hs68 cells were re-suspended in DMEM, counted, and seeded at a density of 20,000 cells·cm^{-2} in the 24-well tissue culture polystyrene (TCPS) plates whose several wells were partly occupied by the PAN NFs. Thereafter, 1 ml medium was added to each well. It is worthy to note that the PAN and c-PAN NFs had been previously sterilized by soaking into alcohol for 30 min and then drying in a laminar flow hood while being UV irradiated for 1 h. The UV sterilization method is commonly used for disinfection of polymeric nanofibers and as reported in the literature, it minimally damages the nanofiber morphology, mechanical properties, and water contact angle [20]. The as-sterilized c-PAN NFs were subsequently biofunctionalized and biomineralized carefully to avoid contamination. After 4 days of incubation, the number of live cells adjacent to the samples was quantified through the WST-1 assay (Roche Applied Science, Mannheim, Germany). The absorbance value was read at 436 nm by a UV–visible absorbance microplate reader (SpectraMax Plus 384, Molecular Devices, Sunnyvale, CA).

Keratinocyte viability was determined through the Alamar Blue assay (Invitrogen, Carlsbad, CA). In this regard, the above procedure was repeated for HaCaT cells (ATCC, Manassas, VA). This time, the cell number was quantified through the Alamar Blue assay. The reduction of Alamar Blue was assessed by fluorescence spectroscopy at a fluorescence excitation wavelength of 560 nm and an emission of 590 nm.

The morphological characteristics of Hs68 cells adjacent to the PAN NFs were determined by immunostaining. The cells were seeded on the NF samples at a density of 20,000 cells·cm^{-2} and cultured in DMEM supplemented with 10% fetal bovine serum and 1% streptomycin/penicillin for 4 days. The cells were subsequently fixed with a 4% paraformaldehyde (PFA) solution and permeabilized by a 1% Triton X-100 solution. Immunostaining of the cells was conducted sequentially with rhodamine–phalloidin (RP, red) and DAPI to visualize the F-actin arrangement and cell nuclei, respectively. The fluorescent images of the stained cells were taken by a fluorescence microscope (Leica DFC360 FX).

2.5. Statistical analysis

One-way analysis of variance (ANOVA) was employed for statistical analysis of the obtained biological data. In this regard, the *p*-values smaller than 0.05 represented a significant difference between the compared data.

3. Results and discussion

The morphology of the neat (SBF treated) and biomineralized PAN NFs is demonstrated in Fig. 2a–c. While the neat PAN NFs are unable to form biominerals, the b-PAN NFs are uniformly covered by a biomineral shell. As seen in Fig. 2c, the biomineral domains spread across the NFs uniformly, implying successful biomineralization of the NFs induced by proper biofunctionalization and homogenous distribution of the protein ligands within the nanostructure. The nanofibers are seen to be beadless and their average diameter was measured to be 316 ± 55 nm (measured by the ImageJ software and based on 70 randomly selected nanofibers' diameter). The diameter does not grow significantly and is measured to be 342 ± 69 nm after biomineralization. Fig. 2d shows the diameter histogram for the two groups of NFs.

To identify the structural and elemental characteristics of the biomineral shell formed on the surface of the PAN NFs, XRD and EDX were employed as two standard related characterization techniques. The XRD pattern of the biomineralized PAN NFs is shown in Fig. 3a. The broad low intensity peak appearing at 2θ = 17.8° in the inset image, implying a low order of crystallinity, is attributed to the (100) crystalline planes of PAN [21–24]. This peak can be also seen in the main spectrum for bm-PAN NFs with a negligible intensity compared to that of the new sharp peaks that appear after biomineralization. The peaks emerging at 2θ = 16.5 and 25° are attributed to the crystalline plane of (101) and (002), respectively, for hydroxyapatite (HA) [25,26]. Such sharp, intense peaks confirm the existence of a large extent of HA crystallites [27].

The HA shell was also characterized via EDX. Based on EDX analysis, Fig. 3b, a Ca/P ratio of ~1.51 can be recorded that implies that a calcium deficient HA (CDHA) has formed on the surface of the NFs

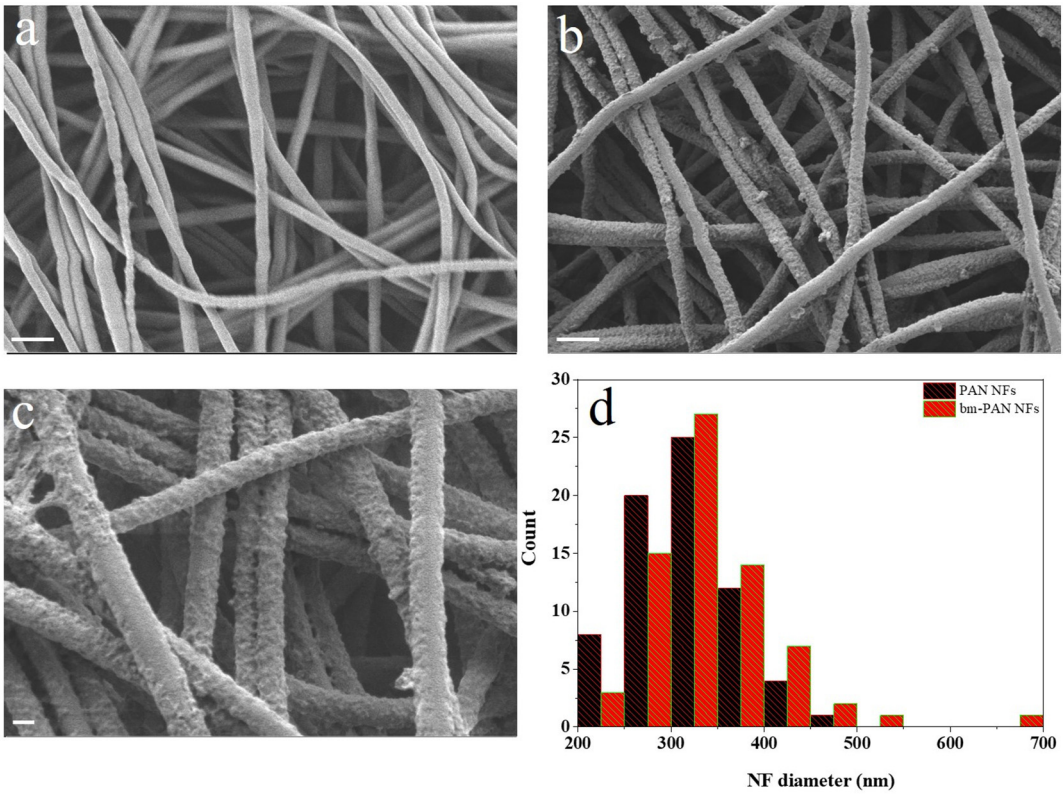

Fig. 2. SEM images imply the morphology of the neat (SBF treated) (a) and biomineralized PAN NFs at two different magnifications (b & c) (the scale bars represent 1 μm (a and b) and 200 nm (c)) (note the uniform biomineral shell formed on the NFs). d) NF diameter histogram for the neat and biomineralized PAN NFs.

[28]. In a similar study, formation of CDHA on biomineralized poly(L-lactic acid)/gelatin NFs has also been reported [29]. Compared to the stoichiometric HA, calcium-deficient HA (Ca_{10-x} $(PO_4)_{6-x}(HPO_4)x$ $(OH)_{2-x}$, $0 \leq x \leq 1$) is of higher biological importance due to its close resemblance to biological HA (seen in bone, e.g.) with the Ca/P ratio of 1.5 [30,31].

The formation process of HA crystals is driven by SBF's neutral pH and thereby the corresponding BSA conformation. At this particular pH condition, the protein is unfolded and Ca^{2+} and PO_4^{3-} ions coexist. Under the isoelectric point of BSA, i.e. 4.7 [32,33], the protein is in its folded state, i.e. "α-helix" whose tryptophan and cysteine residue groups that enable interaction with Ca^{2+}, are mostly hidden within the protein structure and not exposed [34,35]. Also, the peptide groups form strong hydrogen bonds between each other, that render the amine groups unexposed. When the pH rises to neutral, BSA undergoes a conformational change and is unfolded as β-sheet with exposed active groups on the surface. Accordingly, BSA's carboxyl and phosphorous groups acquire highly negative dipoles chelating the free Ca^{2+} cations in the SBF [36]. On the other hand, the PO_4^{3-} ions bond with the protein-reduced calcium, thereby generating the calcium phosphate compound [25].

The different steps of functionalization of the PAN NFs including chemical functionalization (hydrolysis), biofunctionalization and biomineralization, can be tracked in detail through ATR-FTIR, Fig. 3c.

Comparing the graphs related to PAN and c-PAN, it is evident that the intensity of the characteristic peaks at 2243 cm^{-1} (CN stretching) declines for c-PAN, while that of the peak at 1355 cm^{-1} (OH bending) and 1680 cm^{-1} (C═O stretching) rises [37]. On the other hand, the new peaks at 625 cm^{-1} (OH) [38] and 1566 cm^{-1} (amide) emerge. Such changes imply that the nitrile group of PAN is replaced with carboxyl group through the hydrolysis process [39].

The IR graph of b-PAN also shows some alterations when compared with that of c-PAN. The most notable one is the emergence of the amide peaks typical to the protein compounds at 1535 (amide II; δN-H) and 1641 cm^{-1} (amide I; νC═O) [40] and the disappearance of the peak at 1680 cm^{-1} (C═O stretching) as well as the intensity decline of CN group's peak at 2243 cm^{-1} and 1355 cm^{-1} (OH bending). All these changes imply the successful biofunctionalization of the PAN NFs.

When the IR graph of b-PAN and bm-PAN NFs is carefully monitored, it is seen that the characteristic peak of the CN group further declines, the amid bond peak shifts (from 1641 to 1647 cm^{-1}) and a new peak emerges at 2375 cm^{-1} indicating CO_2 adsorbed from the atmosphere [41]. Such alterations could be correlated to the formation of biominerals and the interaction (bonding) between Ca^{2+} and the protein or PAN's functional groups [25]. While the absorption peak at 1641 cm^{-1} is associated with the α-helix structure of the protein, a new shoulder peak appears at 1626 cm^{-1} that represents BSA β-sheet structure [40] and enables biomineralization, as explained before. Normally, dehydration switches back the structure of the protein to its folded one, unless the secondary structure is frozen by interaction and bonding with other elements. This situation is seen in this study and the beta sheet structure partially remains permanently, as indicated in the low intensity shoulder peak.

Thanks to their desirable bioactivity and biocompatibility, biomacromolecules are well-known as modulators of nucleation and growth of biominerals and further for formation of biomineral–polymer composite biomaterials [25]. The BSA protein used in this study is a commercial, inexpensive biomacromolecule, derived from *cow blood,* a widely available byproduct of the *cattle* industry, thus holding promise for large scale production and application. Exposure (immersion) of BSA to SBF i.e. a metastable solution with inorganic ion concentrations almost equal to those in human blood plasma [16] can potentially lead to formation of hydroxyapatite. This phenomenon has been previously reported for silk sericin, for instance [40].

HA nucleation is triggered by the surface functional groups such as carboxyl which are abundant thanks to hydrolysis and

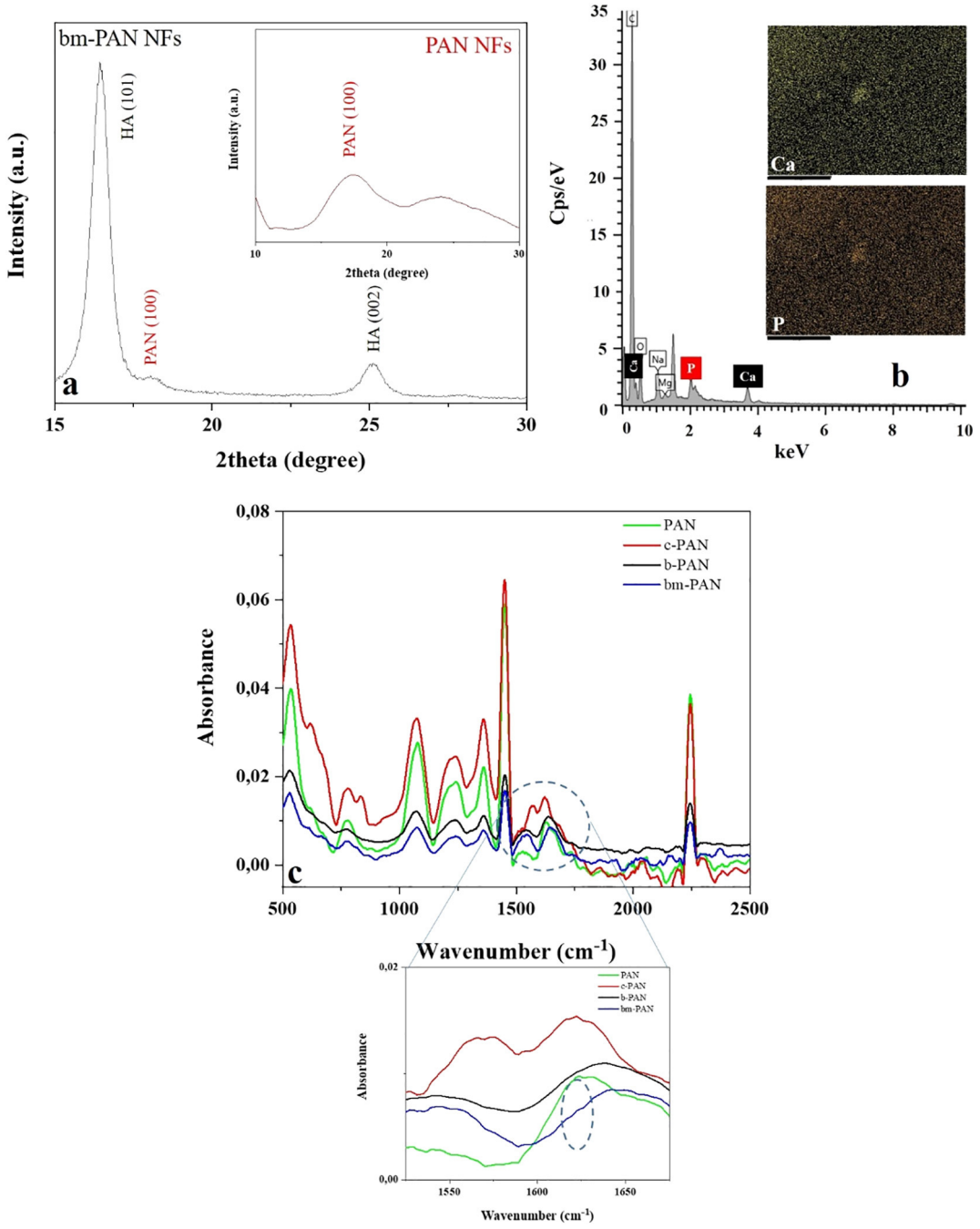

Fig. 3. Chemical analysis of the biomineralized PAN NFs via XRD (a), EDX (b) (Na and Mg originate from SBF. The inset images show distribution of Ca and P elements across the bm-PAN NF mat; the scale bars represent 100 μm), and ATR-FTIR (c). In the latter analysis, a comparison of the spectra for the biomineralized NFs versus those for the neat and functionalized ones confirms successful biofunctionalization and biomineralization of the PAN NFs (the emerging shoulder peak, marked by a circle, represents the remaining β-sheet structure frozen after biomineralization).

biofunctionalization of the NFs. The latter factor, particularly after conformation change of BSA to β-sheet structure, induces the surface functionality of the NFs and affects the arrangement of carboxyl groups. Possessing a β-sheet structure, protein's functional groups in the side chains are trans-arranged top and bottom of the sheet, thereby facilitating HA nucleation [40].

The mentioned functional groups formed through the different functionalization strategies adopted by us could potentially optimize the mechanical properties of the NFs. The inter- and intra-molecular secondary bonding including hydrogen bonding taking place between the functional groups challenges molecular mobility and even movement of NFs relative to each other when subjected to mechanical stresses.

Fig. 4a shows that the elastic modulus of the PAN NFs significantly rises after chemical treatment and biofunctionalization. Especially, the latter approach due to the existence of protein domains between NFs that act as cross-linkers confers the NFs with a notable improvement in stiffness. Such a behavior has been previously reported for a poly(acrylonitrile-*co*-glycidyl methacrylate) (PANGMA) NF membrane biofunctionalized by BSA [35]. In fact, nanometer protein wires interconnect the NFs, thereby increasing the netting points of the web and interfiber bondings, leading to a higher mechanical stability [42,43]. As mentioned earlier, this effect is stressed when the PAN molecules are cross linked within the NFs after functionalization. Thus,

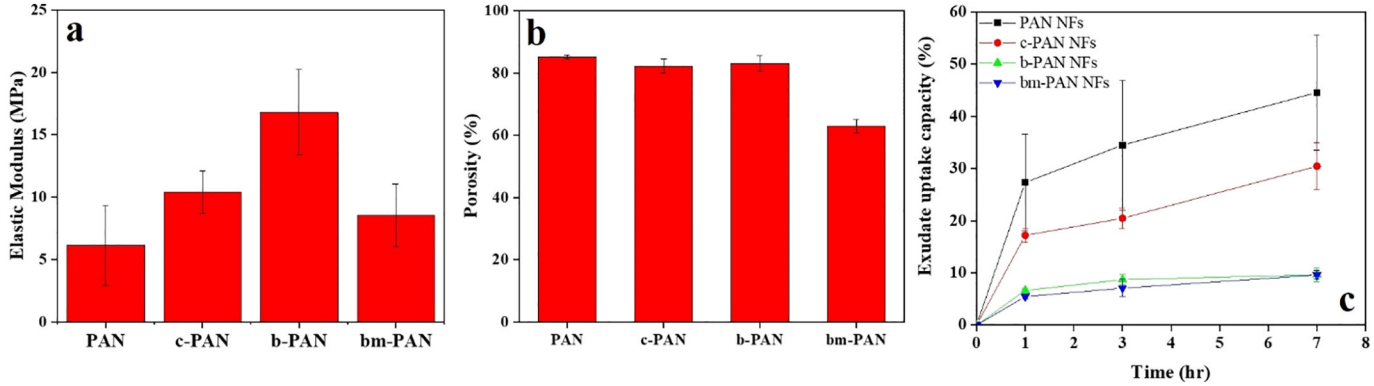

Fig. 4. Structural characteristics of the PAN NFs after hydrolysis (c-PAN), biofunctionalization (b-PAN), and biomineralization (bm-PAN), including elastic modulus (a), porosity (b), and exudate uptake capacity (c).

synergistically, inter/intrafiber bondings lead to a notably higher elastic modulus as 69% (c-PAN), 173% (b-PAN), and 39% (bm-PAN) increase, compared to that of the neat PAN NFs. The reason for the less significant increase of elastic modulus for the biomineralized NFs could be occupation of many functional groups with apatite nuclei and thus the lower contribution of such functional groups to the cross-linking process.

An optimum dressing material should be pliable, elastic and mechanically strong to inhibit additional destruction of the wounded tissue [44,45]. The mechanical properties of wound dressing material also affects cellular activities, owing to high dependency of the cell-matter interplays to the applied shear stresses and mechanical signaling channels that control the migration, proliferation and differentiation of cells [46]. The mechanical characteristics of a wound dressing must match those of the underlying skin tissue to provide analogous biomechanical signals [47]. According to the literature [48], the tensile elastic modulus of human skin ranges from 0.1 to 10 MPa. The elastic modulus of bm-PAN NF dressing is 8.55 ± 2.5 MPa, that optimally lies in this range.

Porosity of the NF mats can largely depend on the extent of biofunctional agents incorporated and the biominerals formed. While according to idealistic calculations done via Eq. (2) and demonstrated in Fig. 4b, the porosity of the PAN NF mat does not decline drastically after hydrolysis and biofunctionalization and remains almost in the same range of 80–85%, it drops down to 63% after biomineralization. However, the actual porosity values of the biofunctionalized and biomineralized NF mats could be lower than those reported here, if we consider the mass fraction of the protein and biomineral, according to the following Eq. (3) [49], and apply the obtained average density in Eq. (2):

$$\frac{1}{\rho} = \frac{\varphi_{PAN}}{\rho_{PAN}} + \frac{\varphi_{BSA\ or\ BSA+Biomineral}}{\rho_{BSA\ or\ BSA+Biomineral}} \quad (3)$$

Given the difficult determination of such quantities in practice, the reported values for both groups of biofunctionalized and biomineralized NFs could be quasi larger than the real values. To validate such a postulate, SEM images of the bm-PAN NF mats were analyzed in terms of porosity by using the ImageJ software. The selected images either indicated presence of the biomineral aggregates (a common observation in the biomineralized nanofiber structures, as will be discussed later) or were free of aggregates. While the porosity measured for the first type of the NF mats was 63–65.5%, the aggregate-free mat showed a large porosity of up to 90%. To be realistic and taking into account the presence of the biomineral aggregates, the lower porosity should be reported, which is surprisingly quite close to the value determined through Eq. (2). However, the porosity calculated by the SEM image analysis is hardly reliable, due to the fact that the selected image shows solely a partial 2D anisotropic surface and cannot accurately represent the 3D porous structure of the entire sample.

The discrepancy between theoretical and practical porosity values is clearly reflected in the exudate uptake capacity of the NF mats. Fig. 4c shows that the highest uptake capacity belongs to the PAN NF mat. In this regard, c-PAN stands in the second place, followed by b-PAN and bm-PAN NF mats.

There is a significant difference in the exudate uptake capacity of the PAN NFs which are surface decorated with protein and biominerals with that of neat or even hydrolyzed PAN NFs. Given the notably high hydrophilicity of all PAN NFs (data not shown here), such a decline in the exudate uptake capacity is mainly associated with the growth of the NFs' diameter due to coating of their surface with protein and biomineral phases. Fig. 5a shows the biomineral shell formed on the

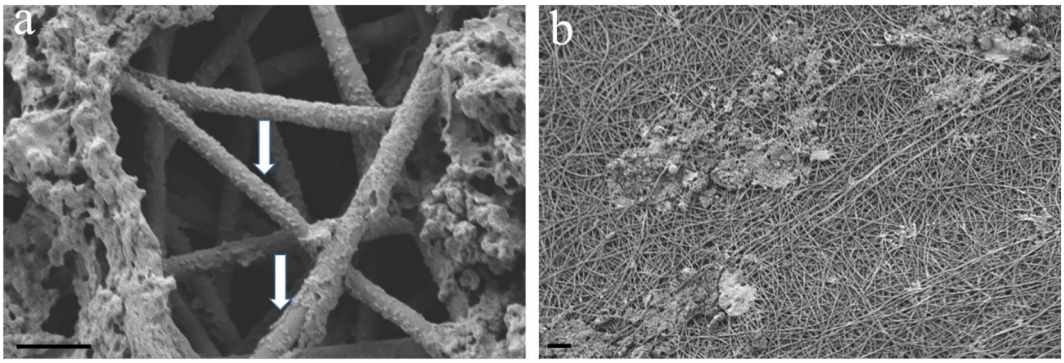

Fig. 5. SEM images show a) the morphology of the bm-PAN NFs as core-shell nanostructures. Here, the uniform distribution of the tiny biominerals across the nanofibers and formation of a shell made of a biomineral phase covering the NFs, marked with arrows, are evident. b) Aggregation of biominerals in some regions can potentially lower the porosity of the NF mat, thereby reducing the exudate uptake capacity (the scale bars represent 1 μm (a) and 10 μm (b)).

surface of the NFs and explicitly implies their diameter expansion. As a result, the pores become smaller in size and porosity drops, leading to a lower exudate uptake capacity. Such a behavior is supplemented by the presence of some dense areas made from biomineral aggregates, that clog the pores. This fact is clearly demonstrated in SEM images, Fig. 5b. The apatite crystals first form on the surface of the NFs, then grow and fill the gap between the fibers. A similar behavior has been reported for k-carrageenan/polyhydroxybutyrate (PHB) NFs after immersion in SBF [50]. This process continues until large micro-sized apatite zones emerge on the NF mats. Formation of the micro-sized biomineral aggregates across nanofibrous mats immersed in SBF for various incubation times has been commonly reported in various relevant researches [27,29,50,51].

The as-developed biomineralized nanofibrous mat comprises nanofiber building blocks with two distinct components of PAN core and CDHA shell. While the biocompatibility of the biomineral phase is widely known in the literature [52–55], the polymer core's effect and in general the synergistic behavior of core-shell materials should be investigated in terms of cell activity and viability. As mentioned earlier, PAN is a rarely studied material for biomedical applications, despite its various merits for industrialization and large scale production.

The morphology and cytoskeletal structure of Hs68 cells adhered on the PAN NFs were imaged by a fluorescence microscope, Fig. 6a–d. According to these images, a larger number of fibroblast cells adheres on the neat and biofunctionalized PAN NF scaffolds than on the biomineralized one. The c-PAN NFs are hydroxylated and thus negatively charged. Considering the same charge for cells, it is plausible that the cells are repelled from these nanofibers [18,56]. Later, upon biofunctionalization, the presence of BSA on the nanofiber surface enables protein-protein interaction and further adhesion of serum proteins, that induces cell adhesion. Moreover, the surface charge shifts to positive thanks to the abundant presence of amine functional groups of the protein component. This charge transition leads to large attraction of the negatively charged cells [57]. Similarly, Kim et al. [57] have verified that a positively charged PCL nanomatrix facilitates adhesion of NIH 3T3 fibroblast cells in comparison with its negatively charged counterpart.

As reported by Keselowsky et al. [58], as one of the major binding sites for adhesion-mediating proteins of the cells surface receptors, fibronectin adsorbs preferably on the surfaces functionalized with NH_3^+ > CH_3 > COO^- > OH. As a result, aminated or carboxylated surfaces show a different behavior in terms of biomolecule adsorption, and thereby tune cell adhesion at different levels [59].

Living cells are also sensitive to the surrounding nanoscale topography and respond accordingly in terms of adhesion and shape [60]. Accordingly, a series of environmental factors such as nanotopography, electrostatic attraction/repulsion, and serum protein absorption modulate cell morphology and adhesion. In the case of the bm-PAN NFs, all the mentioned factors play a role. While the presence of protein endows the nanofibers with a positively charged surface, as seen also for the b-PAN NFs, the calcium phosphate phase is mainly hydroxylated [61] and hides the protein ligands. Thus, a partially negatively charged surface is created that could be slightly repulsive to the cells. On the other hand, formation of the film shaped biomineral aggregate on the surface of the bm-PAN NF mat, even insignificantly, can harm the ECM biomimicry of the NF structure, thus renders it less attractive for cell adhesion.

The morphology of the Hs68 cells seeded onto the PAN NFs was also monitored by SEM after 4 days co-culture. As shown in Fig. 6e–h, the extent of cell coverage for the b-PAN and bm-PAN NFs was higher than that on the neat and c-PAN NFs. The cells exhibited spindle shape and they were shown to stretch across the nanofibrous mats. With respect to the shape of the adhered cells, again the surface charge is decisive. As seen in Fig. 6e–h, the cells take an elongated shape on the negatively charged NFs including c-PAN and bm-PAN, while they are circular and widely spread on the positively charged NFs, i.e. b-PAN NFs. This observation has also been reported by Kim et al. [57]. As schematically shown in Fig. 7a, thanks to the negative charge of the cell membrane, imposing either attractive or repulsive electrostatic interaction with the NF mats with different surface charges, the cells adhere to the surfaces distinctly.

Two main cells involved in the wound healing process are fibroblasts and keratinocytes. The fibroblasts present in the wound area and those derived from blood proliferate and migrate, thereby creating wound granulation tissue and a new ECM. Within the course of wound healing, particularly in the mid and late stages, the interplay of fibroblasts with keratinocytes governs the cellular interactions and transition or upgrade the microenvironment from its inflammatory state to a granulation tissue [62]. Keratinocytes in fact stimulate fibroblasts to synthesize and secrete cytokines and growth factors including keratinocyte growth factor (KGF)/fibroblast growth factor-7 (FGF7), IL-6, and GM-CSF, that play a key role in the wound healing process [62].

In our study, we investigated the viability of such important cells in proximity of the biomineralized PAN NFs. Figs. 7b & c show the viability level of the Hs68 (fibroblast) and HaCaT (keratinocyte) cells co-

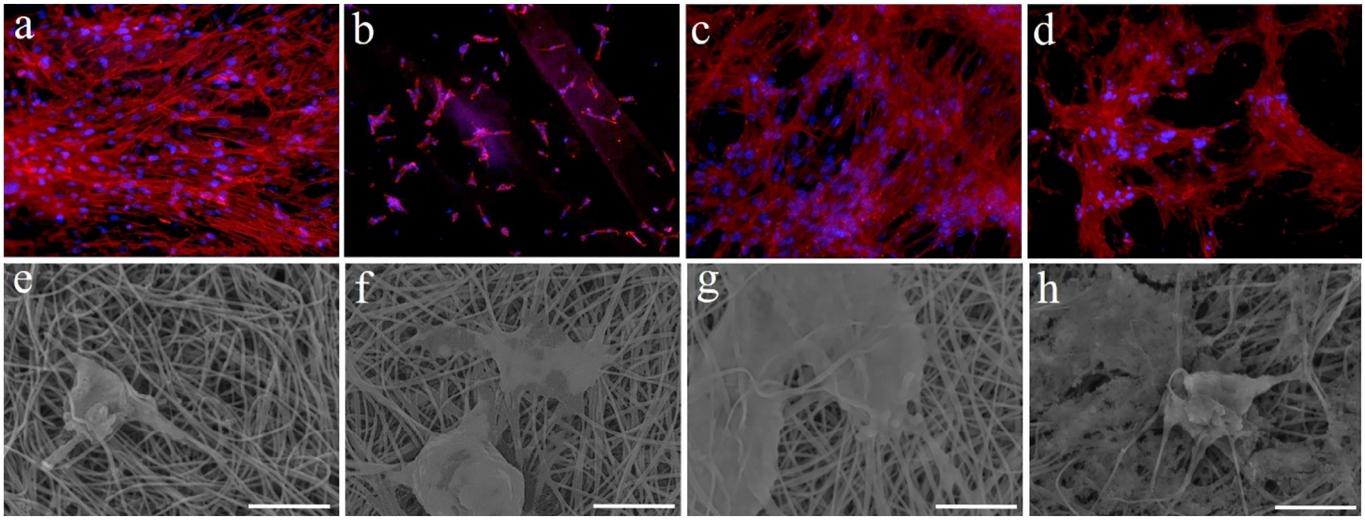

Fig. 6. Merged fluorescent (cellular F-actin (red) and nuclei (blue)) images of Hs68 cells seeded on the PAN NFs as: a) neat, b) hydrolyzed, c) biofunctionalized, and d) biomineralized. SEM images of the Hs68 cells cultured on the PAN NFs as: e) neat, f) hydrolyzed, g) biofunctionalized, and h) biomineralized (the scale bars represent 10 μm). (For interpretation of the references to color in this figure legend, the reader is referred to the web version of this article.)

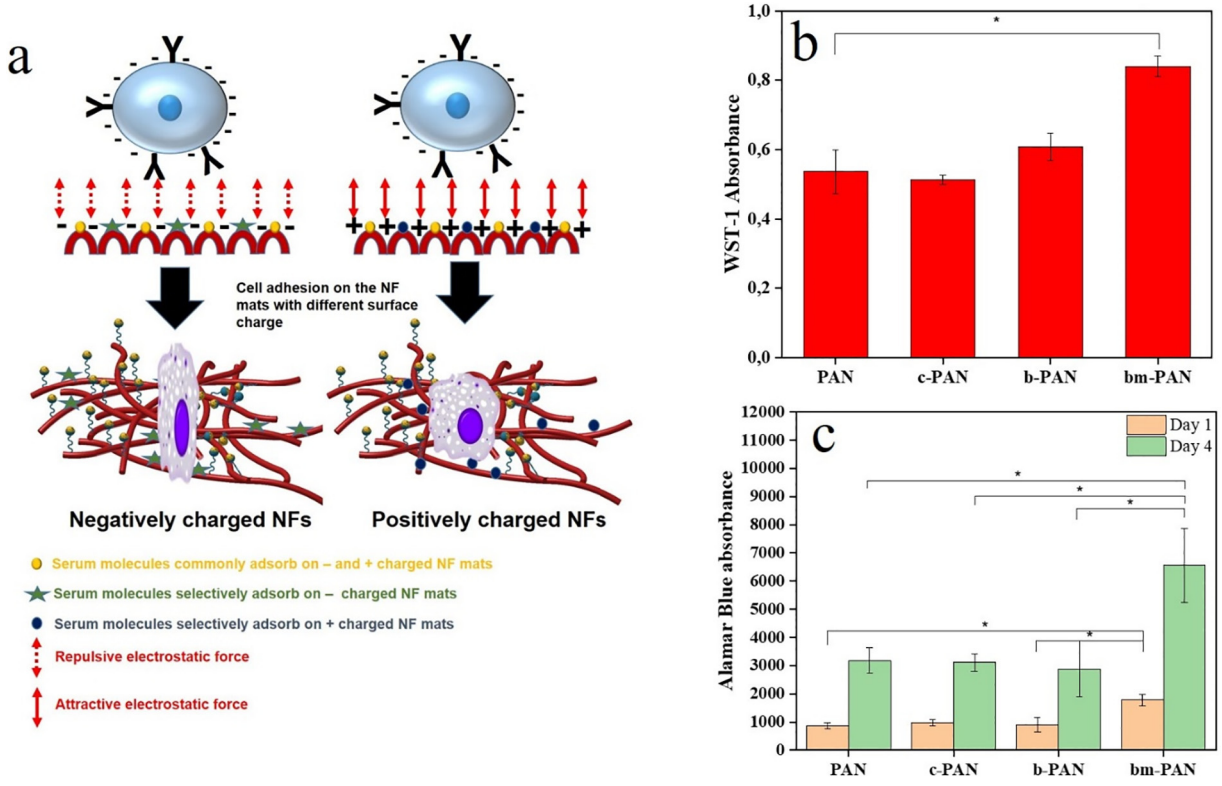

Fig. 7. a) Schematic illustration of the cell adhesion mechanism on NF mats with different surface charges (re-drawn based on a relevant schematic in [57]), b) Hs68 cell viability after 4 days co-culture with PAN NFs with different functionalities, determined via the WST-1 test, c) HaCaT cell viability after 1 and 4 days co-culture with PAN NFs with different functionalities, determined via the Alamar Blue test (the data represent means ± SD (n = 3), *: $p < 0.05$). (For interpretation of the references to color in this figure legend, the reader is referred to the web version of this article.)

cultured with the PAN NFs with different functionality, respectively. After 4 days co-culturing, it is evident that the bm-PAN NFs show a significantly higher cell viability ($p < 0.05$) compared to the neat PAN NFs. In the case of the HaCaT cells as well, such a significant improvement in cell viability (even after 1 day) is observed when comparing bm-PAN NFs with b-PAN and c-PAN NFs.

The ECM comprises an amorphous complex of proteins (collagen, mainly) and polysaccharides, whose interplay leads to establishment of an interconnected nano- or micro-fibrous network. Additionally, the protein fibrilar structure provides a plethora of cell adhesive peptide moieties facilitating cell anchorage [63]. The NF dressing material we synthesized is aimed to mimic the ECM and thereby provoke the cells activity. In terms of structural features, the protein (collagen) fibrils in the natural ECM are as thin as 30–300 nm in diameter [64]. Interestingly, the PAN NFs synthesized in our study are in a similar size range and show an anisotropic arrangement and thus they are able to biomimic the ECM structure and thereby to enable cellular activities.

Despite the fact that the nanofibrous meshes resemble the natural ECM in terms of topography, they need to be equipped with biochemical cues. This prerequisite is met either inherently due to their composition or via biofunctionalization and biomineralization, to induce cellular responses such as adhesion, proliferation, migration, and differentiation. Therefore, a combination of ECM mimicking topography and cell adhesive proteins such as collagen, fibronectin, and laminin can ideally support cell adhesion and proliferation. In contrast to the mentioned proteins, BSA is a non-adhesive protein that is unable to support cell adhesion. However, it can adsorb adhesive proteins such as fibronectin (even at low level) and stimulate cell adhesion and proliferation [65,66]. The adsorbed fibronectin subsequently binds to a certain integrin receptor of cell, $\alpha_5\beta_1$, through its RGD sequence [66]. As reported in the literature [67], the cell adhesion mediated by integrin receptors optimizes cell viability and raises cell proliferation. This behavior was also observed in our study, and the fibroblast cells showed an increased viability in adjacent to the biofunctionalized NFs.

The association of biomineralization of biomaterials (in SBF or after implantation in animal models) to their bioactivity has been widely reported in the literature [68–70]. In this study, the as-formed biomineralized NFs are able to release calcium cations into the cell culture medium, thereby promoting cell proliferation. Positive impact of Ca^{2+} ions on proliferation of hMSCs has been reported by Barradas et al. [71], as well. Ca^{2+} is involved in diverse cellular functions, yet its contribution to such activities has remained elusive [71]. One relevant assumption is that cells sense the extracellular Ca^{2+} through their receptors and respond accordingly, as reflected in their higher activity, gene expression and proliferation [72].

4. Conclusions

Synthetic polymers that can easily be processed through industrial production technologies are promising for development of temporary wound dressings. However, they need to be upgraded with respect to biocompatibility and bioactivity. As mentioned earlier, PAN is a rarely studied material for biomedical applications, despite its various merits for industrialization and large scale production. In this study, we synthesized PAN NF mats that biomimic the natural ECM topographically. Additionally, they were biofunctionalized and then biomineralized to enhance their cell responsiveness. The BSA protein used in this study for the sake of biofunctionalization was a commercial, inexpensive biomacromolecule. The biomineralized PAN NFs stimulated cellular activities and showed improved mechanical properties. Accordingly, a combination of cost-effective and straightforward processing and functionalization as well as optimum biological and mechanical characteristics hold great promise for further study and development of the system investigated here.

Funding sources

European Union's Horizon 2020 research and innovation program under the Marie Sklodowska-Curie grant agreement No. 839165.

CRediT authorship contribution statement

Shahin Homaeigohar: Conceptualization, Methodology, Validation, Formal analysis, Investigation, Writing - original draft, Writing - review & editing, Visualization, Supervision, Funding acquisition. **Ting-Yu Tsai**: Validation, Investigation. **Eman S. Zarie**: Investigation. **Mady Elbahri**: Resources. **Tai-Horng Young**: Resources. **Aldo R. Boccaccini**: Writing - review & editing, Resources, Funding acquisition.

Declaration of competing interest

The authors declare that they have no known competing financial interests or personal relationships that could have appeared to influence the work reported in this paper.

Acknowledgement

S.H. would like to acknowledge the financial support received from the European Union's Horizon 2020 research and innovation program under the Marie Sklodowska-Curie grant agreement No. 839165.

References

[1] http://www.marketsandmarkets.com/Market-Reports/wound-care-market-371.html.
[2] L.I. Moura, A.M. Dias, E. Carvalho, H.C. de Sousa, Recent advances on the development of wound dressings for diabetic foot ulcer treatment—a review, Acta Biomater. 9 (7) (2013) 7093–7114.
[3] L.J. Villarreal-Gómez, J.M. Cornejo-Bravo, R. Vera-Graziano, D. Grande, Electrospinning as a powerful technique for biomedical applications: a critically selected survey, J. Biomater. Sci. Polym. Ed. 27 (2) (2016) 157–176.
[4] V. Andreu, G. Mendoza, M. Arruebo, S. Irusta, Smart dressings based on nanostructured fibers containing natural origin antimicrobial, anti-inflammatory, and regenerative compounds, Materials 8 (8) (2015) 5154–5193.
[5] P. Zahedi, I. Rezaeian, S.O. Ranaei-Siadat, S.H. Jafari, P. Supaphol, A review on wound dressings with an emphasis on electrospun nanofibrous polymeric bandages, Polym. Adv. Technol. 21 (2) (2010) 77–95.
[6] M. Kitsara, O. Agbulut, D. Kontziampasis, Y. Chen, P. Menasché, Fibers for hearts: a critical review on electrospinning for cardiac tissue engineering, Acta Biomater. 48 (2017) 20–40.
[7] A.C. Alavarse, F.W. de Oliveira Silva, J.T. Colque, V.M. da Silva, T. Prieto, E.C. Venancio, J.-J. Bonvent, Tetracycline hydrochloride-loaded electrospun nanofibers mats based on PVA and chitosan for wound dressing, Mater. Sci. Eng. C 77 (2017) 271–281.
[8] Y. Tang, X. Lan, C. Liang, Z. Zhong, R. Xie, Y. Zhou, X. Miao, H. Wang, W. Wang, Honey loaded alginate/PVA nanofibrous membrane as potential bioactive wound dressing, Carbohydr. Polym. 219 (2019) 113–120.
[9] R. Augustine, N. Kalarikkal, S. Thomas, Electrospun PCL membranes incorporated with biosynthesized silver nanoparticles as antibacterial wound dressings, Appl. Nanosci. 6 (3) (2016) 337–344.
[10] H. Skinner, Biominerals, Mineral. Mag. 69 (5) (2005) 621–641.
[11] L. Chen, Y. Liu, C. Lai, R. Berry, K. Tam, Aqueous synthesis and biostabilization of CdS@ ZnS quantum dots for bioimaging applications, Mater. Res. Exp. 2 (10) (2015) 105401.
[12] Y. Bao, Y.S. Tay, T.-T. Lim, R. Wang, R.D. Webster, X. Hu, Polyacrylonitrile (PAN)-induced carbon membrane with in-situ encapsulated cobalt crystal for hybrid peroxymonosulfate oxidation-filtration process: preparation, characterization and performance evaluation, Chem. Eng. J. 373 (2019) 425–436.
[13] Y. Qin, 3 — A brief description of textile fibers, in: Y. Qin (Ed.), Medical Textile Materials, Woodhead Publishing, 2016, pp. 23–42.
[14] M.-C. Yang, J.-H. Tong, Loose ultrafiltration of proteins using hydrolyzed polyacrylonitrile hollow fiber, J. Membr. Sci. 132 (1) (1997) 63–71.
[15] N.-W. Oh, J. Jegal, K.-H. Lee, Preparation and characterization of nanofiltration composite membranes using polyacrylonitrile (PAN). II. Preparation and characterization of polyamide composite membranes, J. Appl. Polym. Sci. 80 (14) (2001) 2729–2736.
[16] T. Kokubo, H. Takadama, How useful is SBF in predicting in vivo bone bioactivity? Biomaterials 27 (15) (2006) 2907–2915.
[17] B. Khabbaz, A. Solouk, H. Mirzadeh, Polyvinyl alcohol/soy protein isolate nanofibrous patch for wound-healing applications, Progr. Biomater. 8 (3) (2019) 185–196.
[18] S. Homaeigohar, T.-Y. Tsai, T.-H. Young, H.J. Yang, Y.-R. Ji, An electroactive alginate hydrogel nanocomposite reinforced by functionalized graphite nanofilaments for neural tissue engineering, Carbohydr. Polym. 224 (2019) 115112.
[19] Polyacrylonitrile, https://en.wikipedia.org/wiki/Polyacrylonitrile.
[20] S. Tort, F.T. Demiröz, S. Yıldız, F. Acartürk, Effects of UV exposure time on nanofiber wound dressing properties during sterilization, J. Pharm. Innov. (2019) 1–8.
[21] S. Homaeigohar, T. Strunskus, J. Strobel, L. Kienle, M. Elbahri, A flexible oxygenated carbographite nanofilamentous buckypaper as an amphiphilic membrane, Adv. Mater. Interfaces 5 (8) (2018) 1800001.
[22] S. Homaeigohar, Amphiphilic oxygenated amorphous carbon-graphite buckypapers with gas sensitivity to polar and non-polar VOCs, Nanomaterials 9 (9) (2019) 1343.
[23] E. Zussman, X. Chen, W. Ding, L. Calabri, D.A. Dikin, J.P. Quintana, R.S. Ruoff, Mechanical and structural characterization of electrospun PAN-derived carbon nanofibers, Carbon 43 (10) (2005) 2175–2185.
[24] J. Bai, Y. Li, S. Yang, J. Du, S. Wang, C. Zhang, Q. Yang, X. Chen, Synthesis of AgCl/PAN composite nanofibres using an electrospinning method, Nanotechnology 18 (30) (2007) 305601.
[25] H. Zhao, W. He, Y. Wang, X. Zhang, Z. Li, S. Yan, W. Zhou, G. Wang, Biomineralization of large hydroxyapatite particles using ovalbumin as biosurfactant, Mater. Lett. 62 (20) (2008) 3603–3605.
[26] W.L. Wijesinghe, M. Mantilaka, R. Rajapakse, H. Pitawala, T. Premachandra, H. Herath, R. Rajapakse, K.U. Wijayantha, Urea-assisted synthesis of hydroxyapatite nanorods from naturally occurring impure apatite rocks for biomedical applications, RSC Adv. 7 (40) (2017) 24806–24812.
[27] Z. Ma, F. Chen, Y.-J. Zhu, T. Cui, X.-Y. Liu, Amorphous calcium phosphate/poly(D,L-lactic acid) composite nanofibers: electrospinning preparation and biomineralization, J. Colloid Interface Sci. 359 (2) (2011) 371–379.
[28] F.C.M. Driessens, M.G. Boltong, E.A.P. de Maeyer, R. Wenz, B. Nies, J.A. Planell, The Ca/P range of nanoapatitic calcium phosphate cements, Biomaterials 23 (19) (2002) 4011–4017.
[29] Q. Cai, Q. Xu, Q. Feng, X. Cao, X. Yang, X. Deng, Biomineralization of electrospun poly(L-lactic acid)/gelatin composite fibrous scaffold by using a supersaturated simulated body fluid with continuous CO_2 bubbling, Appl. Surf. Sci. 257 (23) (2011) 10109–10118.
[30] D.-M. Liu, T. Troczynski, W.J. Tseng, Water-based sol–gel synthesis of hydroxyapatite: process development, Biomaterials 22 (13) (2001) 1721–1730.
[31] H. Begam, B. Kundu, A. Chanda, S.K. Nandi, MG63 osteoblast cell response on Zn doped hydroxyapatite (HAp) with various surface features, Ceram. Int. 43 (4) (2017) 3752–3760.
[32] N. El Kadi, N. Taulier, J. Le Huerou, M. Gindre, W. Urbach, I. Nwigwe, P. Kahn, M. Waks, Unfolding and refolding of bovine serum albumin at acid pH: ultrasound and structural studies, Biophys. J. 91 (9) (2006) 3397–3404.
[33] S. Homaeigohar, T. Dai, M. Elbahri, Biofunctionalized nanofibrous membranes as super separators of protein and enzyme from water, J. Colloid Interface Sci. 406 (0) (2013) 86–93.
[34] D. Zhang, O. Neumann, H. Wang, V.M. Yuwono, A. Barhoumi, M. Perham, J.D. Hartgerink, P. Wittung-Stafshede, N.J. Halas, Gold nanoparticles can induce the formation of protein-based aggregates at physiological pH, Nano Lett. 9 (2) (2009) 666–671.
[35] M. Elbahri, Sh. Homaeigohar, T. Dai, R. Abdelaziz, R. Khalil, A.U. Zillohu, Smart metal-polymer bionanocomposites as omnidirectional plasmonic black absorbers formed by nanofluid filtration, Adv. Funct. Mater. 22 (22) (2012) 4771–4777.
[36] T. Kokubo, H.-M. Kim, M. Kawashita, Novel bioactive materials with different mechanical properties, Biomaterials 24 (13) (2003) 2161–2175.
[37] IR spectrum table & chart, https://www.sigmaaldrich.com/technical-documents/articles/biology/ir-spectrum-table.html (Accessed dec 2019.
[38] J. Reyes-Gasga, E.L. Martínez-Piñeiro, G. Rodríguez-Álvarez, G.E. Tiznado-Orozco, R. García-García, E.F. Brès, XRD and FTIR crystallinity indices in sound human tooth enamel and synthetic hydroxyapatite, Mater. Sci. Eng. C 33 (8) (2013) 4568–4574.
[39] N.-W. Oh, J. Jegal, K.-H. Lee, Preparation and characterization of nanofiltration composite membranes using polyacrylonitrile (PAN). I. Preparation and modification of PAN supports, J. Appl. Polym. Sci. 80 (10) (2001) 1854–1862.
[40] A. Takeuchi, C. Ohtsuki, T. Miyazaki, M. Kamitakahara, S.-i. Ogata, M. Yamazaki, Y. Furutani, H. Kinoshita, M. Tanihara, Heterogeneous nucleation of hydroxyapatite on protein: structural effect of silk sericin, J. R. Soc. Interface 2 (4) (2005) 373–378.
[41] L. Berzina-Cimdina, N. Borodajenko, Research of calcium phosphates using Fourier transform infrared spectroscopy, Infrar. Spectrosc.-Mater. Sci. Eng. Technol. 12 (7) (2012) 251–263.
[42] A. Romo-Uribe, L. Arizmendi, M.E. Romero-Guzman, S. Sepulveda-Guzman, R. Cruz-Silvan, Electrospun nylon nanofibers as effective reinforcement to polyaniline membranes, ACS Appl. Mater. Interfaces 1 (11) (2009) 2502–2508.
[43] S. Bal, Experimental study of mechanical and electrical properties of carbon nanofiber/epoxy composites, Mater. Des. 31 (5) (2010) 2406–2413.
[44] R. Xu, G. Luo, H. Xia, W. He, J. Zhao, B. Liu, J. Tan, J. Zhou, D. Liu, Y. Wang, Novel bilayer wound dressing composed of silicone rubber with particular micropores enhanced wound re-epithelialization and contraction, Biomaterials 40 (2015) 1–11.
[45] S. Homaeigohar, A.R. Boccaccini, Antibacterial biohybrid nanofibers for wound dressings, Acta Biomater. 107 (2020) 25–49.
[46] M.M. Stevens, J.H. George, Exploring and engineering the cell surface interface, Science 310 (5751) (2005) 1135–1138.
[47] D. Chouhan, B. Chakraborty, S.K. Nandi, B.B. Mandal, Role of non-mulberry silk fibroin in deposition and regulation of extracellular matrix towards accelerated wound healing, Acta Biomater. 48 (2017) 157–174.
[48] F. Sun, H.R. Nordli, B. Pukstad, E. Kristofer Gamstedt, G. Chinga-Carrasco,

Mechanical characteristics of nanocellulose-PEG bionanocomposite wound dressings in wet conditions, J. Mech. Behav. Biomed. Mater. 69 (2017) 377–384.
[49] S.Sh. Homaeigohar, H. Mahdavi, M. Elbahri, Extraordinarily water permeable sol gel formed nanocomposite nanofibrous membranes, J. Colloid Interface Sci. 366 (2012) 51–56.
[50] N. Goonoo, B. Khanbabaee, M. Steuber, A. Bhaw-Luximon, U. Jonas, U. Pietsch, D. Jhurry, H. Schönherr, κ-Carrageenan enhances the biomineralization and osteogenic differentiation of electrospun polyhydroxybutyrate and polyhydroxybutyrate valerate fibers, Biomacromolecules 18 (5) (2017) 1563–1573.
[51] Y. Zhang, V.J. Reddy, S.Y. Wong, X. Li, B. Su, S. Ramakrishna, C.T. Lim, Enhanced biomineralization in osteoblasts on a novel electrospun biocomposite nanofibrous substrate of hydroxyapatite/collagen/chitosan, Tissue Eng. A 16 (6) (2010) 1949–1960.
[52] H. Guo, J. Su, J. Wei, H. Kong, C. Liu, Biocompatibility and osteogenicity of degradable Ca-deficient hydroxyapatite scaffolds from calcium phosphate cement for bone tissue engineering, Acta Biomater. 5 (1) (2009) 268–278.
[53] Z. Dai, Y. Li, W. Lu, D. Jiang, H. Li, Y. Yan, G. Lv, A. Yang, In vivo biocompatibility of new nano-calcium-deficient hydroxyapatite/poly-amino acid complex biomaterials, Int. J. Nanomedicine 10 (2015) 6303.
[54] A. Yari Sadi, M.A. Shokrgozar, S.S. Homaeigohar, A. Khavandi, Biological evaluation of partially stabilized zirconia added HA/HDPE composites with osteoblast and fibroblast cell lines, J. Mater. Sci. Mater. Med. 19 (6) (2008) 2359–2365.
[55] A.Y. Sadi, S.S. Homaeigohar, A.R. Khavandi, J. Javadpour, The effect of partially stabilized zirconia on the mechanical properties of the hydroxyapatite–polyethylene composites, J. Mater. Sci. Mater. Med. 15 (8) (2004) 853–858.
[56] C.J. Wilson, R.E. Clegg, D.I. Leavesley, M.J. Pearcy, Mediation of biomaterial–cell interactions by adsorbed proteins: a review, Tissue Eng. 11 (1–2) (2005) 1–18.
[57] J. Kim, D.-H. Kim, K.T. Lim, H. Seonwoo, S.H. Park, Y.-R. Kim, Y. Kim, Y.-H. Choung, P.-H. Choung, J.H. Chung, Charged nanomatrices as efficient platforms for modulating cell adhesion and shape, Tissue Eng. C: Methods 18 (12) (2012) 913–923.
[58] B.G. Keselowsky, D.M. Collard, A.J. García, Surface chemistry modulates focal adhesion composition and signaling through changes in integrin binding, Biomaterials 25 (28) (2004) 5947–5954.
[59] V.A. Schulte, Y. Hu, M. Diez, D. Bünger, M. Möller, M.C. Lensen, A hydrophobic perfluoropolyether elastomer as a patternable biomaterial for cell culture and tissue engineering, Biomaterials 31 (33) (2010) 8583–8595.
[60] T. Dvir, B.P. Timko, D.S. Kohane, R. Langer, Nanotechnological strategies for engineering complex tissues, Nat. Nanotechnol. 6 (1) (2011) 13.
[61] L. Chen, J.M. Mccrate, J.C. Lee, H. Li, The role of surface charge on the uptake and biocompatibility of hydroxyapatite nanoparticles with osteoblast cells, Nanotechnology 22 (10) (2011) 105708.
[62] S. Werner, T. Krieg, H. Smola, Keratinocyte–fibroblast interactions in wound healing, J. Investig. Dermatol. 127 (5) (2007) 998–1008.
[63] T.G. Kim, T.G. Park, Biomimicking extracellular matrix: cell adhesive RGD peptide modified electrospun poly(D,L-lactic-co-glycolic acid) nanofiber mesh, Tissue Eng. 12 (2) (2006) 221–233.
[64] M.C. Alberto-Rincon, T.M. Zorn, P. Abrahamsohn, Diameter increase of collagen fibrils of the mouse endometrium during decidualization, Am. J. Anat. 186 (4) (1989) 417–429.
[65] F. Grinnell, M. Feld, Fibronectin adsorption on hydrophilic and hydrophobic surfaces detected by antibody binding and analyzed during cell adhesion in serum-containing medium, J. Biol. Chem. 257 (9) (1982) 4888–4893.
[66] J.E. Koblinski, M. Wu, B. Demeler, K. Jacob, H.K. Kleinman, Matrix cell adhesion activation by non-adhesion proteins, J. Cell Sci. 118 (13) (2005) 2965–2974.
[67] C.S. Chen, M. Mrksich, S. Huang, G.M. Whitesides, D.E. Ingber, Geometric control of cell life and death, Science 276 (5317) (1997) 1425–1428.
[68] G. Hinata, K. Yoshiba, L. Han, N. Edanami, N. Yoshiba, T. Okiji, Bioactivity and biomineralization ability of calcium silicate-based pulp-capping materials after subcutaneous implantation, Int. Endod. J. 50 (S2) (2017) e40–e51.
[69] N. Sarkar, R. Caicedo, P. Ritwik, R. Moiseyeva, I. Kawashima, Physicochemical basis of the biologic properties of mineral trioxide aggregate, J. Endod. 31 (2) (2005) 97–100.
[70] F.R. Tay, D.H. Pashley, F.A. Rueggeberg, R.J. Loushine, R.N. Weller, Calcium phosphate phase transformation produced by the interaction of the Portland cement component of white mineral trioxide aggregate with a phosphate-containing fluid, J. Endod. 33 (11) (2007) 1347–1351.
[71] A.M.C. Barradas, H.A.M. Fernandes, N. Groen, Y.C. Chai, J. Schrooten, J. van de Peppel, J.P.T.M. van Leeuwen, C.A. van Blitterswijk, J. de Boer, A calcium-induced signaling cascade leading to osteogenic differentiation of human bone marrow-derived mesenchymal stromal cells, Biomaterials 33 (11) (2012) 3205–3215.
[72] T. Matsubara, K. Kida, A. Yamaguchi, K. Hata, F. Ichida, H. Meguro, H. Aburatani, R. Nishimura, T. Yoneda, BMP2 regulates Osterix through Msx2 and Runx2 during osteoblast differentiation, J. Biol. Chem. 283 (43) (2008) 29119–29125.